Chapter 1
Infrared Thermography

Carina Barbosa Pereira, Xinchi Yu, Stephan Dahlmanns, Vladimir Blazek, Steffen Leonhardt, and Daniel Teichmann

Abstract Infrared thermography (also infrared imaging or thermal imaging) is a new remote, non-contact and non-invasive diagnostic and monitoring technique with increasing relevance in a wide range of medical fields. This is mainly due to the several advantages of this technology. Thermal imaging is a passive technique which detects the radiation naturally emitted from an object, in this case the human skin, and does not use any harmful radiation. Thus, infrared thermography (IRT) is suitable for prolonged and repeated use. In the last decades, new medical applications for thermal imaging have arisen. These techniques have been successfully used in the diagnosis of several pathologies, including breast cancer, rheumatic diseases, dry eye syndrome, vascular diseases, etc. Infrared thermography has also demonstrated its potential in the monitoring of several vital signs, including temperature, respiratory rate, heart rate, and blood perfusion. Recently, there has been new advance in 3D infrared imaging. A three-dimensional thermal signature may provide several advantages in the detection and monitoring of the course of several pathologies including arthritis, thyroid dysfunctions, breast cancer, sports lesions, and diabetic foot. The current chapter focuses on advances in the area of medical IRT. First, it reviews the basics of IRT and essential theoretical background. Second, some medical applications and corresponding methods are

---

Carina Barbosa Pereira, Xinchi Yu, and Stephan Dahlmanns contributed equally to this work.

C. Barbosa Pereira (✉) · X. Yu · S. Dahlmanns · S. Leonhardt · D. Teichmann
Chair for Medical Information Technology, Helmholtz-Institute for Biomedical Engineering, RWTH Aachen University, Aachen, Germany
e-mail: pereira@hia.rwth-aachen.de

V. Blazek
Chair for Medical Information Technology, Helmholtz-Institute for Biomedical Engineering, RWTH Aachen University, Aachen, Germany

Czech Institute of Informatics, Robotics and Cybernetics (CIIRC), Czech Technical University in Prague, Prague, Czech Republic

M. Abreu de Souza et al. (eds.), *Multi-Modality Imaging*,
https://doi.org/10.1007/978-3-319-98974-7_1

described in detail. Third, it gives an overview on the recent advances on "3D Infrared Thermography".

Keywords Infrared thermography · Medical applications · Diagnostic · Monitoring · 3D infrared thermography

1.1 Introduction

Infrared thermography (IRT), also known as thermal imaging, is an imaging modality, which senses infrared radiation (heat) emitted by objects. In contrast to other imaging techniques in medicine, such as X-Ray, computed tomography (CT), and magnetic resonance imaging (MRI), IRT is a completely passive—i.e., non-invasive and non-radiating—measurement technique. The first infrared thermogram of a human was recorded in 1928 by Prof. Czerny in Frankfurt, Germany [1]. Initially, only single infrared detectors have been used. Later on, during World War II, infrared detectors have been developed and used for military applications [2]. Besides the issues regarding availability (military restrictions) and price, that technology was unsuitable for medical applications: both thermal resolution (approx. 0.5 K) and spatial resolution (approx. 5 mm at a target size of 50 cm^2) were too low in order to detect small temperature differences and anatomic structures on the human body. Moreover, the infrared detectors were big and needed cooling by, e.g., nitrogen, argon gas, or a sterling cooler [3]. It was only in the 1990s and early 2000s when the development and availability of uncooled microbolometer focal plane arrays (FPA) pioneered the usage of IRT in medicine. In contrast to the old devices with single detectors, the new cameras with FPAs provided a high spatial and thermal resolution. Also temporal resolution (sample rate or scanning speed) increased, enabling real-time and high-speed recordings. Another factor was the availability of computers and more user-friendly image processing software [3, 4].

A widely known medical application of modern IRT is mass fever screening during worldwide pandemics, for example, at airports. With the general trend in medicine away from a reactive, curative approach (diagnosis and treatment) towards a proactive and preventive approach (identification of risks and elimination of those), IRT is playing an important role. Since it can easily detect anomalies of body surface temperature, i.e., hyperthermia due to inflammation or hypothermia induced by poor perfusion, there are multiple medical applications [4]. In this chapter, we will introduce some of them—detection of breast cancer, diagnosis of rheumatic diseases, dry eye syndrome, wounds, monitoring of vital sings (respiratory rate, cardiac pulse, and perfusion) as well as the capabilities of 3D thermal imaging.

1.2 Physical Principles of Infrared Thermography

Thermographic cameras are unable to sense the surface temperature of an object directly. Rather, the power of electromagnetic rays that hit the sensors of the cameras is measured. In this section the physical principles for the calculation of the surface temperature from its radiation are introduced. Additionally, the effects of non-ideal objects as well as effects of the transport medium in medical applications of thermographic measurements will be considered.

1.2.1 Thermal Radiation

All objects with a surface temperature above absolute zero (0 K or −273.15 °C, respectively) emit electromagnetic radiation with a particular wavelength (λ). This phenomenon is different from heat transfer due to the collusion of particles, called conduction, where the energy transport depends on the temperature gradient inside the transport medium. Radiation, on the other hand, describes the energy transfer by electromagnetic waves, which is solely dependent on the temperature of the radiation source. For example, the electromagnetic radiation of the sun reaches Earth even though the temperature of outer space is constant.

The theory of radiant heat was first described by Max Planck in 1913 and is the fundamental basis of the calculation of surface temperatures based on the spectral analysis of its radiation [5].

1.2.2 Blackbody Radiation

A practical way to describe the energy flux of radiation is via an idealized physical body called "blackbody". A blackbody absorbs all incident radiant energy without reflection and is homogeneous as well as isotropic. Hence, its radiation is emitted uniformly in all directions of space. In addition, it is postulated that all radiation of a blackbody is entirely dependent on the body's absolute temperature, therefore the phenomena of luminescence are excluded from calculations. In order to describe thermal radiation, the permanent state will be investigated, which means that the energy and thus the temperature of the blackbody are distributed equally inside its volume.

Based on these assumptions, it is possible to calculate the spectral distribution of thermal radiation emitted by a blackbody. This function was first described by Max Planck as the Planck spectrum M_λ^0 and follows the equation:

$$M_\lambda^0(\lambda, T) = \frac{2\pi hc^2}{\lambda^5 \cdot (e^{\frac{hc}{\lambda kT}} - 1)}. \tag{1.1}$$

Fig. 1.1 Spectral radiant exitance of a body (M_λ^0) at two different temperatures: 300 and 5778 K (surface temperature of the sun)

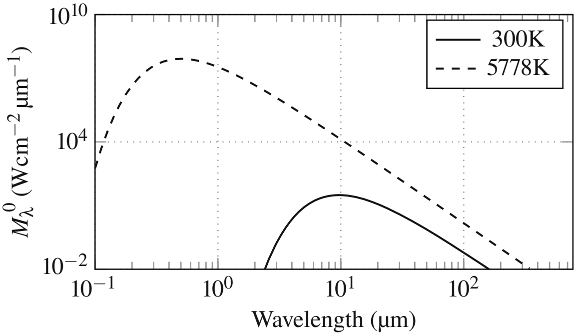

Here, M_λ^0 represents the spectral radiant exitance of the blackbody in (W m^{-2} µm^{-1}), λ is the wavelength (µm), T stands for the surface temperature (K), h denotes the Planck constant ($h = 6.626 \times 10^{-34}$ J s), $k = 1.3807 \times 10^{-23}$ J K^{-1} corresponds to the Boltzmann constant, and $c = 2.998 \times 10^8$ m s^{-1} is the speed of light in vacuum. M_λ^0 is a function of λ, which means that the total energy content is distributed over a range of wavelengths. This resulting energy distribution is dependent on the temperature T of the blackbody as displayed in Fig. 1.1.

The shape of the Planck spectrum is similar for all temperatures, but its amount of power as well as the wavelength of maximum power ($\lambda_{\max}$) is shifted based on the surface temperature. For example, the surface temperature of the sun equals 5778 K; this creates a spectrum with a wavelength of maximum power at around $\lambda_{\max} \approx$ 500 nm (the wavelength where human eyes evolved to be most sensitive ranges between about 390 and 700 nm). Bodies with surface temperatures around 300 K (26.85 °C) generate a Planck spectrum between 2.5 and 150 µm. As temperature decreases, the radiation emitted is more in the range of longer wavelengths. This effect is explained by Wien's displacement law. Wavelengths created by surface temperatures of around 300 K are invisible for the human eye, but sensors that are sensitive around 10 µm are able to detect this radiation, just like human eyes can detect the radiation emitted by the sun [6].

Surface temperatures can be calculated based on the total radiant power per surface area M (W m^{-2}). Hence, it is not necessary for thermal detectors to distinguish between different wavelengths. In general, M describes the area underneath the curves given in Fig. 1.1; it can be calculated by integrating M_λ^0 over the range of all significant wavelengths as given by

$$M = \int_{\lambda^0=0}^{\infty} M_\lambda^0 \, \mathrm{d}\lambda. \tag{1.2}$$

The solution of the integral can be estimated by applying the Stefan-Boltzmann law:

$$M = \sigma \cdot T^4, \tag{1.3}$$

where $\sigma = 5.67 \times 10^{-8}$ W m^{-2} K^{-4} is the Stefan-Boltzmann constant. With this equation the surface temperature of an object can be easily calculated based on the measurement of the radiated power per surface area. This is the general working principle of sensors integrated in thermographic cameras.

1.2.3 Greybody Radiation

Both Planck's and Stefan-Boltzmann's law describe the radiation of a blackbody under ideal conditions. Nevertheless, real bodies often do not absorb all radiant energy. In general, objects interact in three different ways with radiation: by absorption (α), reflection (β), and transmission (γ). Considering the law of conservation of energy, $\alpha + \beta + \gamma = 1$ applies. For black bodies, the absorption value α equals 1 and reflection and transmission are zero. If the absorption value is less than 1, the considered object is called a "greybody". Solid bodies are generally opaque (transmission $\gamma = 0$), and consequently $\alpha + \beta = 1$.

According to Kirchhoff's law, at a given temperature the ratio of radiant absorbance to emittance is constant for greybodies ($\alpha = \epsilon$), therefore the emissivity for each wavelength is described by

$$\epsilon = 1 - \beta_\lambda. \tag{1.4}$$

For greybodies the Stefan-Boltzmann law takes the form

$$M = \epsilon \cdot \sigma \cdot T^4, \tag{1.5}$$

where ϵ is constant for all wavelengths. Since ϵ is smaller than 1 for greybodies, their temperature has to be larger to create the same total radiant power of blackbodies.

1.2.4 Temperature Measurement

As mentioned previously, thermal cameras measure and convert the radiation energy emitted by a body into a temperature value. However, not all radiation detected by the camera sensors corresponds to the target object. The measured energy (W_{tot}) rather consists of the emission of the object (E_{obj}) plus reflected emission from ambient sources (E_{amb}) and emission from the atmosphere (E_{atm}).

The atmosphere describes the transport medium of heat radiation. In this medium, there are molecules that interact with the heat rays: some of its energy gets absorbed or scattered and the atmospheric transmittance γ_{atm} must be considered. Therefore, the Stefan-Boltzmann law for black bodies in vacuum,

$$M_{\mathrm{measured}} = \sigma \cdot T_{\mathrm{obj}}^4, \tag{1.6}$$

Table 1.1 Parameters used to calculate the temperature of the target object T_{obj}

Parameter	Symbol	Value
Total radiant power	M_{measured}	Measured by the camera
Emittance of object	ϵ_{obj}	Unknown/estimated
Transmittance of atmosphere	γ_{atm}	Approximated: $\gamma_{\mathrm{atm}} \cong 1$
Stefan-Boltzmann constant	σ	$5.67 \times 10^{-8}\,\mathrm{W\,m^{-2}\,K^{-4}}$
Temperature of ambient objects	T_{amb}	Unknown
Temperature of the atmosphere	T_{atm}	Unknown

must be adapted for greybodies in the atmosphere:

$$M_{\mathrm{measured}} = \epsilon_{\mathrm{obj}} \cdot \gamma_{\mathrm{atm}} \cdot \sigma \cdot T_{\mathrm{obj}}^4 + (1 - \epsilon_{\mathrm{obj}}) \cdot \gamma_{\mathrm{atm}} \cdot \sigma \cdot T_{\mathrm{amb}}^4 + (1 - \gamma_{\mathrm{atm}}) \cdot \sigma \cdot T_{\mathrm{atm}}^4. \quad (1.7)$$

The parameters necessary to compute the temperature of the target object T_{obj} are displayed in Table 1.1. Next to the Stefan-Boltzmann constant σ and the measured radiation M_{measured}, additional information about the object itself (namely, object's emittance ϵ_{obj}) and its environment (such as temperature of the atmosphere T_{atm}, temperature of ambient objects T_{amb}, and transmittance of the atmosphere γ_{atm}) need to be known.

The transmittance of a medium can vary very strongly for different wavelengths. For example, visible light propagates through water with few losses (you can see very far in clear water) in contrast to infrared light that is completely absorbed by the water molecules. The transmittance for wavelengths above 1500 nm approximates zero. This makes impossible the use of IRT under water. The transmittance of air γ_{atm} is dependent on the wavelength as well. As opposed to water, there exists a transmittance window that makes thermography possible. For a significant range of wavelengths, γ_{atm} is approximately 1. Thus, when air is the transport medium, Eq. (1.7) can be further simplified

$$M_{\mathrm{measured}} \cong \epsilon_{\mathrm{obj}} \cdot \sigma \cdot T_{\mathrm{obj}}^4 + (1 - \epsilon_{\mathrm{obj}}) \cdot \sigma \cdot T_{\mathrm{amb}}^4. \quad (1.8)$$

Now, the relation between measured power and the object's temperature is independent from air temperature.

There are many sources of thermal radiation that could increase the thermal radiation without increasing the object's temperature, for example, the sun, heating or light bulbs, especially when the emissivity of the greybody is noticeably below 1. In practice, the operator of a thermal camera should make sure that there are no ambient heat radiation sources close to the object of interest. In this case the equation further simplifies to

$$M_{\mathrm{measured}} \cong \epsilon_{\mathrm{obj}}. \quad (1.9)$$

Finally, in order to correctly calculate a surface temperature based on the radiation, the emissivity ϵ_{obj} of the object needs to be known. Many thermal cameras give the option to input the emissivity value of the object that is currently measured. However, this value is often unknown or multiple objects with different emissivity values are measured at the same time. The consequences are systematic measurement errors that distort the results, i.e., the output of the camera.

In medical applications, the surface area of interest often consists of human skin. Its emissivity ϵ_{skin} is well known, approximately 0.97–0.99 for temperatures around 300 K. Therefore, blackbody theory can be applied for the measurement of skin surface temperatures. In contrast, the emissivity of inner organs like the heart is noticeably below 1. This has to be considered for surgical applications of thermal imaging [7, 8].

1.2.5 Thermal Cameras

There are multiple types of thermal detectors capable of converting infrared radiation into electrical signals. For medical applications, these systems need to be saved, easy to use, and inexpensive. Traditionally, thermographic cameras have been used for maintenance and research especially in industrial processes, like engine diagnostics or power electronics. These cameras are capable of covering a thermal range from values below 0 °C up to temperatures far above 1000 °C and use detectors that often require active cooling. Additionally, the lenses of most thermal cameras cannot to be made of glass whose transmissivity approaches zero for wavelengths above 4500 nm. Hence, rare materials such as Germanium or sapphire crystals need to be incorporated.

Cameras for standard clinical applications use sensors that cover the wavelength spectrum from 3 to 5 µm (mid-wave infrared) and from 7 to 14 µm (long wave infrared), and therefore the bulk of the Planck spectrum of human skin temperatures (around 300 K). They reach temporal resolutions of 30 frames per second (fps) and make the analysis of dynamic temperature changes possible.

Thermographic cameras do not reach the spatial resolution of modern cameras in the visible spectrum, primarily because the sensor technology, active cooling, and materials for lenses are very expensive. High sensitivity hand-held infrared cameras reach resolutions of 2048 × 1536 pixels. Today, there are standard thermographic cameras on the market that do not require cooling and reach resolutions of 1024 × 768 pixels. Those camera types are often used for medical applications that will be further described in Sect. 1.3. Cameras for standard clinical applications use modern sensor technologies like microbolometer disposed on FPAs. These technologies reach thermal sensitivities below 0.1 °C, and their accuracy lies around 1 °C. They enable the analysis of small temperature changes on the surface of an object, like the temperature distribution on the human skin [9]. Nevertheless, the thermal accuracy of infrared cameras does not allow for sophisticated diagnostics of absolute temperatures, especially when the effects of unknown emissivities (as described above) are taken into account [10, 11].

1.3 Medical Applications

In the last decades several medical applications for thermal imaging cameras started to emerge. The next sections present some of the current applications of IRT for both medical fields, diagnosis and monitoring.

1.3.1 Diagnosis

A healthy human body presents a symmetric temperature distribution around the sagittal plane [12]. However, there are several biological factors that might influence the human body temperature, locally or systemically. Therefore, any deviation from normal can be an indicator of pathophysiologic anomalies, such as inflammation, carcinogenesis, or neuropathology [13]. The first use of temperature for health assessment dates back to 400 BC in the writings of Hippocrates. Hippocrates routinely slathered wet mud and clay over the patients' bodies speculating that the areas where the mud dried first had a disease [14]. Abnormal thermal patterns can be easily recognized in thermal imaging. Therefore, an early diagnosis of certain diseases is possible through the analysis of thermograms. In the last couple of years, IRT has found a wide acceptance among the medical community due to its advantages. Thermal imaging is a remote, non-contact, non-invasive, and passive technique. It only records the natural radiation emanated from the skin surfaces and does not use any harmful radiation [2, 15]. Lastly, IRT is a real-time technology, enabling monitoring of dynamic variations of body temperature. Due to all these advantages, thermal imaging has been considered an effective alternative diagnosis tool [2]. It has been being used in a variety of medical applications, including fields such as neurology, oncology, orthopedics, and dermatology [16]. Table 1.2 describes some medical applications, relevant research studies, and the hardware used. In the following sections only four applications will be presented in detail.

1.3.1.1 Detection of Breast Abnormalities

According to the World Health Organization, 1.7 million breast cancer cases occurred in 2012 worldwide. It is the most frequent cancer in women in 150 countries (approximately 25% of all cancer cases) as well as the most common cause of cancer-related death. It was estimated that 522,000 women died from this cancer in 2012 worldwide [38]. Studies demonstrated that an early detection can lead to 85% survival chance while a late detection of breast cancer leads to only 10%. Therefore, it is very important for physicians to identify in due course potentially threatening malignant tumors for a successful treatment [2]. Mammography is the current gold standard to examine the human breast. However, this technique exhibits low sensitivity in young women and in women with a

Table 1.2 Medical applications of IRT (Ref.—references)

Application	Year	Authors [Ref.]	IRT system
Breast cancer	2011	Kontos et al. [17]	Meditherm Med2000™ Pro (Meditherm, Medical Monitoring Systems Pty Ltd., Beaufort, NC, USA)
	2011	Umadevi et al. [18]	Fluke Ti40FT (M/s Fluke Corp., Everett, Washington, USA) and Varioscan 3021 ST (InfraTec GmbH, Dresden, Germany)
Complex regional pain syndrome	2006	Niehof et al. [19]	ThermaCam SC2000 (FLIR, Danderyd, Sweden)
	2008	Gardiner et al. [20]	FLIR A40M (FLIR Systems Boston, MA, USA)
	2016	Cho et al. [21]	IRIS-5000 (Medicore Co., Seoul, Korea)
Diabetic neuropathic foot	2006	Bharara et al. [22]	Unknown
Dry eye syndrome	2010	Tan et al. [23]	VarioCAM, JENOPTIK Laser (Germany)
	2017	Matteoli et al. [24]	FLIR 320A (FLIR Systems, Oregon, USA)
Knee injuries	2010	Hildebrandt et al. [4]	TVS-500EX (NEC Avio Infrared Technologies, Tokyo, Japan)
Low back pain	2006	Zaproudina et al. [25]	IRTIS-2000 C (IRTIS Ltd, Moscow, Russia)
Osteoarthritis	1981	Ring et al. [26]	Unknown
	2004	Varju et al. [27]	Compix PC2000e (Compix, Lake Oswego, OR, USA)
	2010	Denoble et al. [28]	Meditherm Med2000™ Pro (Meditherm, Medical Monitoring Systems Pty Ltd., Beaufort, NC, USA)
Peripheral arterial disease	2009	Bagavathiappan et al. [29]	AGEMA Thermovision 550 system (Danderyd, Sweden)
	2011	Huang et al. [30]	Spectrum 9000-MB Series (United Integrated Service Co. Ltd, Taipei Hsien, Taiwan)
	2016	Staffa et al. [31]	FLIR B200 (Flir Systems, Danderyd, Sweden)
Raynaud's phenomena	2014	Lim et al. [32]	IRIS-XP® (Medicore, Seoul)
Rheumatoid arthritis	2015	Lasanen et al. [33]	FLIR A325 (FLIR Systems Inc., USA)
	2017	Lerkvaleekul et al. [34]	FLIR E60 (FLIR System Inc., USA)
Shoulder impingement syndrome	2007	Park et al. [35]	IRIS 5000 (Medicore, Seoul, Korea)
Wound assessment	2015	Dini et al. [36]	FLIR T620 Thermal Imager (FLIR Systems Boston, MA, USA)
	2017	Keenan et al. [37]	FLIR A325 (FLIR Systems Boston, MA, USA)

greater breast density. In addition, this technique requires breast compression during screening and exposes the patient to harmful radiation (X-rays usually around 30 kVp). Several studies have demonstrated that thermal imaging may be a potential adjunctive tool for detecting this kind of cancer [38]. Breast thermography was firstly introduced by Lawson in 1956 [39]. According to this author, one of the biological characteristics of malignant tumors is the increased rate of growth in comparison to that of the surrounding tissues. This leads to an accelerated local metabolism, which is supported by increased blood and lymphatic vascularity, and consequently to localized hot spots [2, 39]. Amalric et al. screened over a period of 10 years 61,000 women using thermography [40]. Their outstanding study showed that thermal imaging was the earliest marker of breast cancer in approximately 60% of the cases [40]. In addition to passive breast imaging, there are other procedures to enhance thermographic contrast of tumors. The first is based on cold stimulation. The blood vessels which supply the tumors are simply endothelial tubes devoid of a muscular layer. Thus, during cold stress (sympathetic stimulus) they fail to vasoconstrict and show instead a hyperthermic pattern due to vasodilation [2]. The second procedure is based on induced evaporation. Deng and Liu [41] demonstrated that this technique enhances the temperature contrast in case of tumors underneath the skin. In short, the authors sprayed water and 75% of ethanol solution (evaporant) before imaging acquisition. They conclude that this method permitted to improve diagnostic accuracy, particularly in the early stage of deeply embedded tumors [41].

In 2012, Boquete et al. proposed a novel approach capable of detecting high tumor risk areas [42]. It was based on independent component analysis. For validation purposes, they used the database of the *Ann Arbor thermography center* comprising eight case studies, where two out of eight were control cases. The thermograms had YCbCr 480 × 380 pixels format and followed a color code: lower temperatures were shown in blue and higher temperatures in yellow-red tones; the highest temperatures were displayed in white. While Fig. 1.2a shows a control case, Fig. 1.2b, c denotes two cases of ductal carcinoma. The proposed method corroborated that the hot spots in the thermogram of the breast indicate a potentially cancerous zone. It presented a sensitivity of 100% and specificity of 94.7%. The positive and negative predictive values were 83% and 100%, respectively [42].

1.3.1.2 Rheumatic Diseases

Rheumatic diseases are a group of over 150 systemic autoimmune diseases (e.g., rheumatic arthritis, osteoarthritis and autoimmune diseases, such as systemic lupus erythematosus, scleroderma, osteoporosis, back pain, gout, fibromyalgia, and tendonitis) which are characterized by inflammation affecting the connecting or supporting structures of the body, mostly joints, but also tendons, ligaments, bones, and muscles. Common symptoms of these diseases include swelling, pain, stiffness, and decreased range of motion. Rheumatic diseases are one of the leading causes of disability in the USA affecting more than 50 million people of all ages, genders, and races. By 2040, the number of adults in the USA is expected to increase to 78.4 million.

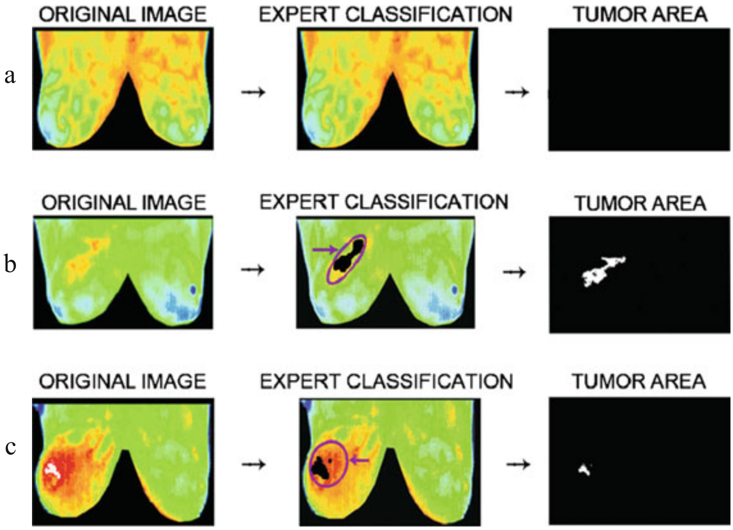

Fig. 1.2 (**a**) Control case. (**b**, **c**) Ductal carcinoma. Modified from Boquete et al. [42]

Currently, there are few tools for early diagnosis of rheumatic diseases and for assessing the effectiveness of therapies: bone scintigraphy, ultrasound, contrast enhanced ultrasound, magnetic resonance (MR), and contrast enhanced MR. However, these techniques are not readily available for the masses and waiting lists in many countries are very long. Therefore, less expensive technologies for diagnosis and therapy monitoring would be beneficial in this medical field.

IRT has been used in the diagnosis and assessment of recovery of some rheumatic diseases, including Raynaud's phenomena, gout, and arthritis [2]. In an outstanding publication, Ring [43] demonstrated that patients suffering from juvenile arthritis,[1] osteoarthrosis,[2] rheumatoid arthritis,[3] gout,[4] among others show abnormal temperature distributions over joints. To quantify joint inflammation, Collins et al. [44] developed in 1974 a "thermographic index":

---

[1] Juvenile arthritis, also known as pediatric rheumatic disease, is an umbrella term that describes autoimmune and inflammatory conditions or pediatric rheumatic diseases developed in children under the age of 16.

[2] Osteoarthrosis is the most frequent chronic condition of the joints, affecting more than 30 million Americans. It can affect any joint, but it occurs most commonly in knees, hips, lower back and neck, small joints of the fingers, among others.

[3] Rheumatoid arthritis is an autoimmune disease in which the body's immune system mistakenly attacks the joints.

[4] Gout is a form of inflammatory arthritis that affects people who have high levels of uric acid in the blood. Uric acid can form needle-like crystals in the joints. The most common symptoms are sudden and severe episodes of pain, tenderness, redness, warmth, and swelling.

$$\frac{\sum(\Delta t \times a)}{A}, \tag{1.10}$$

where Δt stands for the difference between the measured isothermal temperature and a constant (26 °C); a is the area occupied by isotherm (region of the thermogram with the same temperature); and A corresponds to the total area of the thermogram. In other study, Ring et al. [45] studied the ability of thermal imaging to detect and quantify the effects of non-steroidal anti-inflammatory drugs (such as aspirin, indomethacin, and benorylate) in patients with gout and rheumatoid arthritis [45]. The results indicated that IRT is a suitable tool for assessment of the response to the anti-inflammatory treatment; the administration of a local anti-inflammatory caused a fall in the thermographic index of the inflamed joint. Frize et al. used, in turn, IRT for diagnosis of rheumatoid arthritis [46]. The authors reported that metacarpophalangeal joints of the index, middle fingers, and knee are the best indicators of the presence and absence of this disease [46]. Lerkvaleekul et al. studied the capability of IRT to detect wrist arthritis in juvenile idiopathic arthritis patients [34]. Using the mean temperature and maximum temperature at the skin surface in the region of interest, moderate wrist joint arthritis could be differentiated from severe and inactive arthritis. In 2009, Wu et al. published a work where they claimed that local skin temperature near the coccyx region decreases significantly after therapy in patients suffering from coccygodynia (pain in the coccyx or tailbone area) [47]. In this case, thermal imaging has demonstrated to be an effective tool for the assessment of coccygeal pain intensity after treatment. In contrast, Park et al. used IRT for the assessment of shoulder impingement syndrome [35]. They prospectively evaluated 100 patients with unilateral impingement syndrome, and a control group of 30 subjects. In IRT findings, 73% of the patients presented abnormal thermal changes, 51% displayed hypothermia, and 22% had hyperthermia. The results confirmed that in the hypothermic group limitation of shoulder motion was significantly more prominent than in the other groups: hyperthermic and normal groups. Commonly, shoulder immobility induces a localized muscle atrophy, which in turn causes apoptosis of the muscle's cells. This phenomenon may lead to a decreased blood flow in this region, resulting in hypothermic patterns in the skin of the shoulder [35]. Vecchio and associates [48] corroborated in their papers the findings of Park et al. [35]. They stated that the most part of the subjects with unilateral frozen shoulder had anomalous skin temperature distribution [48].

1.3.1.3 Dry Eye Syndrome and Ocular Disease

Dry eye syndrome is a disturbance of the tear film caused by a lack of adequate tears. Tears can be described as a complex mixture of water, mucus, and fatty oils, which make the surface of the eyes smother and clear and protect them from infection. Therefore, dry eye syndrome may lead to eye inflammation, vision problems, as well as scarring on the surface of the corneas.

Nowadays, there are some methods for diagnosis of dry eye. Film breakup time and tear osmolarity give information about tear functionality but do not specify the causes of possible damage. The objective clinical examination of corneal fluorescein staining may help in the diagnosis but is very fastidious.

In recent decades, the diagnostic of dry eye syndrome and ocular diseases using infrared thermography has been analyzed. Studies have demonstrated that patients with dry eye disease have cooler ocular surfaces than those of asymptomatic normal subjects [24, 49]. In 2009, Tan and associates [23] published a review paper describing different methodologies for manual, semi-manual, and automatic measure of ocular surface temperature in IRT.

Additionally, thermal imaging can be used for diagnosis and assessment of the inflammatory state in patients with Graves' ophthalmopathy as described by Chang et al. [50]. Note that Graves' orbitopathy is an autoimmune inflammatory disorder of the orbit and periorbital tissues. It is characterized by lid lag, upper eyelid retraction, conjunctivitis, redness, among others. In their study, the authors measured the temperature at different regions, including lateral orbit (reference point), cornea, medial and lateral conjunctiva, upper and lower eyelids, and caruncle. They observed significantly higher temperature differences between reference point and other eye regions for the patients suffering from this inflammatory disorder [50].

1.3.1.4 Wound Assessment

A chronic wound is commonly defined as a wound whose healing process is hampered. Commonly, wounds are classified as chronic if they need more than 3 months to heal, i.e., to recover anatomic and functional integrity. Indeed, they may require several years to heal, and in some cases remain unhealed for decades. Patients with this problem can experience pain, reduced mobility, physical and emotional distress as well as social isolation. The Wound Healing Society classifies chronic wounds into four categories: diabetic ulcers, pressure ulcers, venous ulcers, and arterial insufficiency ulcers [51].

In the USA, chronic wounds affect approximately 6.5 million patients ($\sim$2% of the US population) leading to annual costs of about 25 billion US dollars. In the Scandinavian countries, the associated medical costs correspond to 2–4% of the total health care expenses. However, the medical expenditures are increasing rapidly due to aged population and a sharp grow in the incidence of diabetes and obesity worldwide [51].

Thermal imaging can be used for non-invasive assessment of wound severity. The potential of IRT to aid in the assessment of wounds was identified by Lawson in the early 1960s [52]. He used this technology to predict burn depth. Histological analysis confirmed an accuracy of 90%. The author stated that whereas superficial burns are warmer than uninjured skin due to increased inflammatory processes, deeper burns are cooler than uninjured skin owing to structural damage of the vasculature [52]. In 1996, Hansen et al. [53] published a very interesting work where they studied the capability of IRT to assess wound severity of newly formed temperature-modulated pressure injuries in a porcine model. They observed that relative surface temperature of the wounds strongly correlated with the presence or absence of deep tissue injury. In addition, infrared imaging permitted to assess wound depth and, thus, predict the severity of the injuries.

The measurement of skin and wound bed temperature in chronic wounds may play an important role in the assessment and diagnosis of chronic wound infection. Dini et al. [36] carried out a study whose aim was to correlate the wound bed score,[5] validated by Falanga [54] in 2006, to wound bed and perilesional skin temperature. It included 18 patients suffering from venous insufficiency and lower leg ulcers. In total, 24 chronic wound bed and perilesional skin ulcers were assessed using an infrared thermographic camera (FLIR T620 Thermal Imager, FLIR Systems, Boston, Massachusetts, USA). The authors conclude that wound bed temperature plays a major role in wound healing. According to them, if the temperature of the wound bed falls below the core body temperature, healing can be delayed due to lack of collagen deposition and reduced amount of late-phase inflammatory cells as well as fibroblasts [36] . Fierheller and Sibbald [55], in turn, studied the importance of periwound skin temperature. They demonstrated a statistically significant relationship between infection and increased periwound skin temperature [55].

1.3.2 Monitoring

In the last decade, thermal imaging has been used for monitoring of vital signs, such as respiratory rate (RR) and heart rate (HR), and perfusion dynamics. Possible applications are monitoring of preterm infants in neonatal intensive care units as well as critical care patients in intensive care units. Additionally, this monitoring technology can be used in the automotive branch as well for continuous monitoring of drivers. The following sections discuss the capability of IRT as a monitoring technique.

1.3.2.1 Respiratory Rate

Respiratory rate (RR) is an important vital sign and is measured in breaths per minute or min^{-1}. Each breath or breathing cycle consists of two phases: inspiration and expiration. During inspiration, the diaphragm contracts and moves towards the caudal (downward) direction; due to under pressure in the pleural cavity the lungs are also pulled towards the caudal direction and air is sucked into the

---

[5] The wound bed score is based on healing edges (wound edge effect), presence of eschar, greatest wound depth/granulation tissue, amount of exudate amount, edema, periwound dermatitis, periwound callus and or fibrosis, and a pink/red wound bed.

lungs. Simultaneously, the rib cage moves towards the cranial and ventral (up and forward) direction in order to accommodate the increased volume of the lungs. This movement is also translated to the shoulders. During expiration, the diaphragm relaxes; the lungs and ribcage also move back into the relaxed end-expiratory position and warm air is exhaled.

Usually the RR of an average adult under resting conditions ranges from 12 to 20 breaths per minute (min^{-1}). An abnormal RR, such as bradypnea (low RR, $<12\,\text{min}^{-1}$) or tachypnea (increased RR, $>20\,\text{min}^{-1}$), can be the first indication for various medical conditions including heart and lung diseases. Furthermore, analysis of the respiration pattern can provide even more information. Kussmaul's respiration, for example, which is characterized by deep breaths at normal or low RRs, can point towards a diabetic coma or kidney failure. Another example is Cheyne–Stokes respiration, which is characterized by alternating phases of hyperpnea and apnea. Additionally, the depth of the breaths increases at the beginning of the hyperpnea phase and decreases again towards the end. Underlying reasons for Cheyne–Stokes respiration can include cardiac insufficiency and cerebral damage. Despite all the information carried in the RR and respiratory pattern, it is still an often neglected parameter [56]. A study of Philip and associates [57] showed that both spot and formal assessment of RR performed by physician is sometimes highly inaccurate and that they were not able to detect abnormal RRs. The findings of this study emphasize the importance of techniques in order to reliably and easily detect RR [57].

Technical state-of-the-art for respiration monitoring includes impedance pneumography (measurement of respiration-modulated thoracic impedance), spirometry (flow measurement), capnography (measurement of exhaled carbon dioxide), piezoplethysmography (measurement of thoracic and/or abdominal effort), and thermistors (measurement of respiration-modulated temperature differences around the nostrils). All these methods rely on sensors, which need to be directly attached to the patient and usually have cables to, e.g., a patient monitor. These factors limit both patient comfort and ease of use, which is why there have been many efforts to develop non-contact methods for RR monitoring in the recent years. Among other techniques, the application of IRT for non-contact respiration monitoring has been investigated intensively.

In 2004, Murthy, Pavlidis, and Tsiamyrtzis first proposed IRT for touchless monitoring of breathing function [58]. In a dimly lit room, the faces of ten subjects were recorded in a profile view using a mid-wave infrared camera with a spectral range of 3.0–5.0 μm, a spatial resolution of 640×512 pixels, and a temperature sensitivity of 25 mK. Temperature changes caused by inhalation and exhalation were measured in a region of interest (ROI) a certain distance away from the nose tip. In order to determine the RR, those temperature modulations were first classified as either part of the inspiration or part of the expiration phase using statistical distributions. Afterwards, the RR could be derived from the length of the respiration cycles. This work was later extended by Fei and Pavlidis in 2007 [59] and 2010 [60]. Table 1.3 lists other works on the field of respiration monitoring using IRT.

Table 1.3 Works on the field of respiration monitoring using IRT

Year	Authors	Summary	Reference
2005	Chekmenev et al.	Measurement of RR on 4 healthy subjects by analysis of temperature variations around the nose and wavelets for signal processing and analysis	[61]
2008	Yang et al.	Estimation of RR on 20 healthy subjects using temperature modulations measured around the nose and fast Fourier transform for signal processing and analysis	[62]
2009	Murthy et al.	Airflow monitoring on 14 healthy adult subjects and 13 adult sleep apnea patients using temperature modulations around the nose and wavelets for signal processing and analysis	[63]
2011	Abbas et al.	Monitoring of RR on seven premature infants in a hospital using temperature variations around the nostrils and wavelets for signal processing and analysis	[64]
2011	Al-Khalidi et al.	Peak detection on temperature changes around the nose for RR monitoring on 16 children	[65]
2011	Lewis et al.	Extraction of RR and relative tidal volume on 25 healthy subjects based on temperature modulations around the nose and fast Fourier transform for signal processing and analysis	[66]
2015	Pereira et al.	Monitoring of respiration dynamics on 11 healthy subjects by analysis of temperature changes around the nose and a robust interval estimator	[67]

Although the algorithms and experimental settings of the works listed in Table 1.3 differ from each other, a general structure is clearly visible: after acquisition of thermal video sequences, the image frames undergo *image preprocessing* and *image enhancement*, before *selection of a ROI*. To compensate motion, a *tracking algorithm* is applied to the ROI. Then, *extraction of the respiration waveform* from the ROI is performed and, finally, the *RR is calculated*. The following pages will focus on image processing, image enhancement, selection of ROI, extraction of respiration waveform, and calculation of RR. Tracking algorithms are not covered in this section, thus the reader is kindly referred to the original research articles.

Selection of ROI

Research listed in Table 1.3 uses the area around the nose as the ROI. There, the temperature variation between inspiration and expiration, which lies around 0.3–0.6 K for adults, is measured (see Fig. 1.3). In the work of Murthy et al., subjects were recorded in a profile view [58]. Their approach consisted in: (1) removing the background with the Otsu's method; (2) detecting the nose tip (regarded as the right most point); and defining a ROI (region direct below the nose tip). After experimental evaluation, considering the distance between subject and camera as

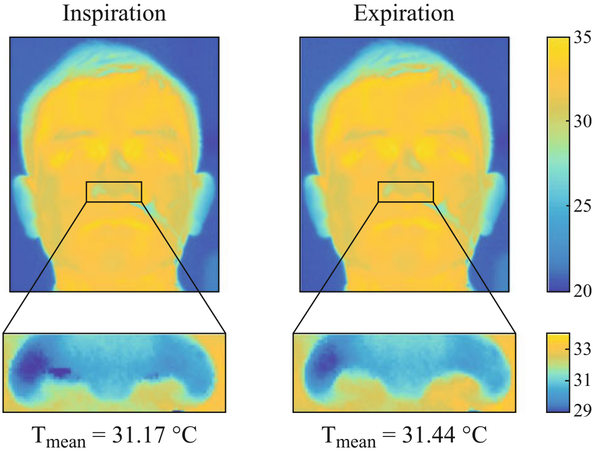

Fig. 1.3 Temperature differences around the nostrils between inspiration and expiration

well as the lens' focal length, the size of the ROI was set to 21 × 9 pixels. In a later version of their work, Fei and Pavlidis [60] recorded the subjects in a frontal view and used a semi-automatic approach in order to detect the nose. Initially, the area around the nose is manually selected in the first frame of the video and then tracked throughout the whole video sequence by a tracker. Within this tracked ROI (TROI), the exact position of the nostrils is automatically detected. This is accomplished by application of both the horizontal and vertical Sobel Operator to the TROI, which detects the spatial features of the nostril area. By calculation of the horizontal as well as vertical projection of the edge image, the boundaries of the nostrils are clearly visible and can be obtained.

Another approach was proposed by Al-Khalidi et al., which first segments the face of the subject recorded from a frontal perspective and detects the two warmest points in the face [65]. Due to the facial temperature distribution, those points coincide with the periorbital regions. From there downwards, the coldest point is the tip of the nose.

However, although commonly used, the nose is not the only suitable region in order to extract a respiration waveform. Another suitable ROI is the mouth. Al Khalidi et al., for example, had to exclude four subjects from analysis, since they were breathing through the mouth [65]. In 2016, Pereira et al. presented a robust algorithm for estimation of RR [68]. In addition to the nose, the mouth and both shoulders were added as ROIs. While the respiration waveform around the nose and mouth was caused by temperature changes during inspiration and expiration, the respiration waveform around the shoulders was induced by respiration-related movement of the shoulders. Respiratory rate was estimated independently for each ROI and fused afterwards; different fusion algorithms (Bayesian fusion, median, and a signal quality-based algorithm) were investigated.

Extraction of Respiration Waveform and Calculation of Respiratory Rate

The respiration waveform is usually obtained from the 2D average temperature over time according to Eq. (1.11)

$$s(t) = \frac{1}{XY} \sum_{x=1}^{X} \sum_{y=1}^{Y} I(x, y, t), \tag{1.11}$$

with $s(t)$ being the respiration waveform at time t and $I(x, y, t)$ the value at position (x, y) of the infrared video frame at time t. Based on this respiration waveform, the RR can be determined by many forms of signal processing and signal analysis. One frequently used method is continuous wavelet transform (CWT) according to Eq. (1.12)

$$W_{\psi,s}(a, \tau) = \frac{1}{\sqrt{|a|}} \int \psi \left(\frac{t - \tau}{a} \right) s(t) \, \mathrm{d}t, \tag{1.12}$$

where a is the scaling parameter, τ represents the translation parameter, ψ denotes the mother wavelet, and s is the signal to be analyzed. Fei and Pavlidis [60], for example, used the Mexican hat wavelet as mother wavelet and assume that the RR is represented by the scale $a_{\max}$ with maximum energy. Finally, the RR is calculated according to

$$\mathrm{RR} = \frac{F_c \cdot fs}{a_{\max}}, \tag{1.13}$$

where F_c is the center frequency of the mother wavelet and fs is the sampling rate of the respiration waveform. Abbas et al. use the Daubechies wavelet as the mother wavelet instead of the Mexican hat [64].

Another method for calculation of the RR is the short time Fourier transform (STFT), given by

$$S(\omega, \tau) = \int s(t) \cdot w(t - \tau) \cdot e^{-j\omega t} \, \mathrm{d}t. \tag{1.14}$$

Here s is the signal to be transformed and w is a windowing function (e.g., Hamming, Hann, Gaussian window). The window size must be chosen carefully with regard to temporal and spectral resolution. Zero padding can be applied in order to increase the number of frequency points in the spectrum and therefore increase the precision of peaks within the spectrum. However, it should be noted that zero padding does not increase the spectral resolution. Afterwards, the RR can be obtained from the spectrum by selecting the frequency with maximum spectral energy. This method was used by Lewis et al. [66] and Pereira et al. [68].

There are other techniques to determine RR from the respiration waveform, for instance, (1) bandpass-filtering of the respiratory waveform and calculation of the time peak-to-peak [65] or (2) using a robust breath-to-breath interval estimator [67].

In the publication of Murthy et al., the average RR obtained with IRT was compared with the RR measured by a piezo belt (reference). On average, an accuracy of 92% (over ten healthy subjects) was obtained [58]. In the work of Yang et al. the absolute deviations ranged from 0.8 to 2.2 breaths/min between average IRT respiratory rate and average ground truth [62]. In 2011, Abbas et al. first measured RR with IRT on five premature neonates in a neonatal intensive care unit [64]. The average deviation between average IRT respiratory rate and reference respiratory rate was approximately 1 breaths/min and the largest average deviation was 2.25 breaths/min. In 2016, Pereira et al. used fusion of multiple ROIs for RR estimation [68]. Among others, they investigated the effects of different breathing patterns on the algorithm's performance. To validate the approach, an experiment on 12 healthy subjects was conducted. For normal breathing, the root mean squared error (RMSE) was 0.28 breaths/min and correlation between IRT respiratory rate and ground truth was 0.98 (averaged over all 12 subjects). For the simulated respiration patterns, RMSE averaged 3.36 breaths/min and the correlation was 0.95. The increased RMSE could be explained by an imperfect time synchronization between IRT and ground truth in combination with rapid changes of RRs. In total, both lab experiments and clinical studies indicate that IRT is a very promising method for RR monitoring.

1.3.2.2 Cardiac Pulse

In addition to RR, some research groups studied the capability of IRT to monitor the cardiac pulse [69, 70]. In 2007, Garbey et al. proposed a novel method to monitor HR at a distance [70]. Their aim was to develop a non-invasive and contactless method capable of assessing the human anatomic nervous system activity and psychophysiology state. According to them, in psychophysiological experiments, the physiological responses of a subject should be measured without any interfere, otherwise an extra variable must be introduced to his psychological state. In these cases, a contact-free measurement modality for monitoring of vital signs (e.g., RR and cardiac pulse) is very appealing [70]. Such measurement methodology can also be beneficial in critical care medicine, especially in the monitoring of burned and traumatized patients as well as premature infants [68].

As well known, during ventricular systole the heart contracts generating blood pressure and flow fluctuations that propagate as waves through the arterial tree [71]. The approach proposed by Garbey and associates [70] is based on the hypothesis that pulsative blood flow modulates temperature of surrounding tissues (e.g., skin) as a result of heat exchange by convection and conduction (between vessels and surrounding tissue). Certainly, this modulation is more pronounced in the vicinity of greater blood vessels. To verify the hypothesis, the authors implemented a mathematical model to simulate the heat transfer processes on the skin, including the influence of core tissue and major superficial blood vessels. The simulations showed that the skin temperature waveform is similar to the pulse waveform; the amplitude of the temperature variation ranged between 0.02 and 0.03 °C [70].

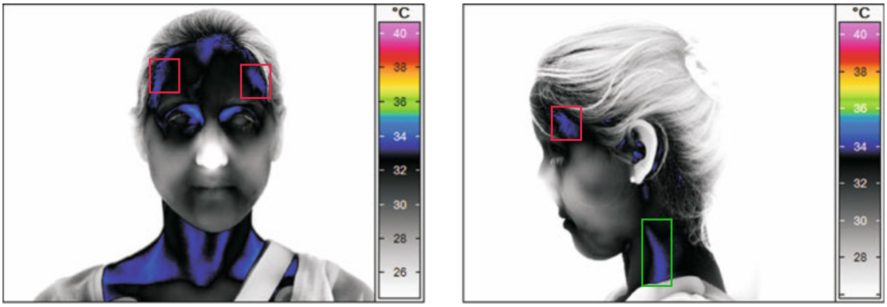

Fig. 1.4 Regions where the cardiac pulse can be extracted using thermal imagery: superficial temporal vessel complex (red boxes) and carotid vessel complex (green box)

Due to tissue thermal diffusion, variation of skin temperature is strongest along the superficial blood vessels, as demonstrated in [30]. Based on that assumption, Garbey et al. focus their research on three different body regions: neck (external carotid complex), temporal area (superficial temporal artero-venous complex), and wrist (radial artero-venous complex) [70]. Figure 1.4 shows two of these regions: red boxes enclose the temporal vessel complex and the green box encloses the carotid vessel complex. As displayed the blood vessels are hot spots in the thermogram. In short, the approach of this research group consisted in manually selecting a "line-based region" (ROI) along visible vessels in the first frame of thermal video. To compensate involuntary movements of the subjects, a motion tracking algorithm was integrated; the authors chose the conditional density propagation tracker with thresholding as its feedback mechanism. Then, they applied the fast Fourier transform (FFT) to the individual pixels along the line of interest to capitalize upon the pulse propagation phenomenon. As a blood vessel is a long and narrow structure, the pulse's thermal propagation effect induces a slight phase shift on the temperature profile along it. Within this context, each single pixel along the line of interest has a unique periodic temperature profile, which was considered to be shifted with regard to the others. Thus, the temperature profiles of the pixels are shifted in the time domain but not in the frequency domain. Lastly, an adaptive estimation function was applied on the average FFT outcome to extract the dominant pulse frequency [70].

To validate their approach, the authors carried out experiments on 34 healthy human subjects using a high sensitive mid-wave infrared camera from FLIR (FLIR Inc., Santa Barbara, CA). It presents a temperature resolution of <25 mK and a full spatial resolution of 640 × 480 pixels. Thermal videos (5 min) were acquired with a frame rate of 30 fps. The HR obtained with thermal imaging was compared to a standard ground-truth (GT), a piezoelectric transducer [70]. On average, the performance of the method, given by complement of the absolute normalized difference (CAND),[6] was 88.52%.

---

[6] $\text{CAND} = 1 - \frac{|\text{GT}-\text{IRT}|}{\text{GT}}$, where GT corresponds to the HR obtained with the ground truth and IRT stands for the HR estimated with infrared thermography.

A research group of the University of Louisville (Louisville, Kentucky, USA) proposed a similar approach to that of Garbey et al. [70]. In 2007, Chekmenev et al. developed a multi-resolution method for non-contact measurement of the arterial pulse [69]. In general, the algorithm detects in the ROI the skin area where the arterial periodic heat pattern is more prominent. Then, multiscale decomposition models are applied to each frame in order to extract the scales containing most of the arterial pulse information. As a result, the influence of irrelevant noise is minimized and a better accuracy can be achieved. The next step consists in selecting the coarse scales to track the ROI. Afterwards, the ROI is divided into K-cells and the mean temperature value is calculated; this results in K one-dimensional waveforms. For each waveform, continuous waveform analysis is applied to detect systolic peaks/maxima for each single waveform; this method permits to remove high frequency noise and to extract arterial pulse structures. Finally, the waveform with higher periodicity is used to calculate the cardiac pulse; the cell corresponding to this waveform is defined as region of measurement [69].

To validate the approach, measurements on five healthy subjects were carried out. The research group used a long-wave Phoenix infrared camera from FLIR (FLIR Inc., Santa Barbara, California, USA) with the following characteristics: thermal sensitivity of 25 mK; 14-bit dynamic range; spatial resolution of 320 × 256 pixels. In this experiment the acquisition time ranged between 20 and 50 s and the frame rate was 30 fps. The HR obtained with IRT was compared to a standard ground truth (GT), a portable HR monitor from Polar USA. According to the authors, a 100% accuracy on the carotid artery area was obtained [69].

In 2013, the same research group presented a full-automatic approach to estimate the pulse signal. In contrast to the previous works, the new algorithm identifies the forehead in the thermogram and extracts the vascular maps (Fig. 1.5). Every vessel segmented in the forehead is then used to calculate the HR [72].

In this work an experiment with 32 subjects was carried out. Here, three different scenarios were tested. In the first scenario (phase A—normal condition), the thermal videos were recorded during normal conditions. During phase B (second scenario—

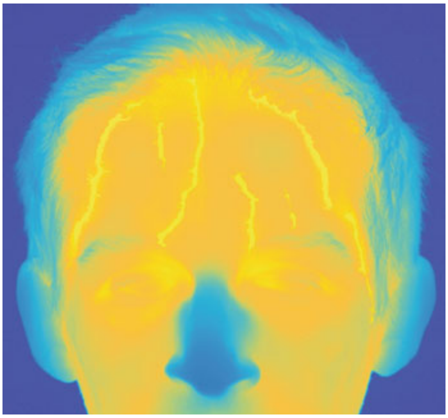

Fig. 1.5 Thermal facial region and vascular maps of the forehead

mild pain), the healthy subjects submerged their right hand in an ice bath to induce pain. In the last phase (phase C—mild exercise), subjects held 20–40 lbs of weight in order to increase HR [72].

The results showed an overall accuracy of almost 90% (median). Under normal conditions, the best outcome was achieved, the median averaged 92.5%. In phase B (pain) and phase C (mild exercise) the median was approximately 91% and 82%, respectively [72].

1.3.2.3 Perfusion

Acute circulatory disorders are still one of the main causes of death worldwide. In critical care medicine, this complication is frequently triggered by sepsis or SIRS (systemic inflammatory response syndrome). Sepsis is considered a severe disease consisting of both infection and SIRS. It may evolve into severe sepsis or septic shock. Whereas the first is an aggravated sepsis by acute organ dysfunction, the second corresponds to a severe sepsis plus hypotension, which cannot be settled with fluid resuscitation [73, 74].

According to the World Health Organization (WHO), severe sepsis and septic shock are the main factors of morbidity and mortality in intensive care units [75] and neonatal intensive care units [76]. In the USA, approximately 751,000 cases of severe sepsis occur annually with a mortality rate of 28.6%. This estimation was presented by Angus et al. in 2001 [77]. In 2003, Martin and associates observed an increase in septicemia incidence and septicemia-related deaths over the past 20 years in the USA [78]. This trend is expected to continue due to several reasons including aging of the population, increasing number of immunosuppressive therapies, transplantations, chemotherapies, and invasive procedures [79]. Furthermore, a study carried out by Lawn et al. [80] evidenced that severe infections such as sepsis/pneumonia, tetanus, and diarrhea are the second major cause of dead in neonates at the age of 0–27 days. According to the publication, of 3.072 million deaths in 2010, approximately 27% were due to severe infections [80].

During sepsis cardiovascular changes are patent. Commonly, they lead to tissue hypoperfusion, which can further result in the development of multiple organ dysfunction. Thus, to improve the outcome of the patients through appropriate clinical interventions (e.g., antibiotic therapy and organ support) the diagnosis must be performed in due course [73, 81]. The remarkable work of Kumar et al. evidenced an increase of circa 7.6% in mortality rate for every single hour by which antimicrobial was tardily administered [82]. However, a prompt identification of sepsis is still a major challenge for clinicians as its signs and symptoms are nonspecific [82].

Body temperature, and consequently skin temperature, is dependent on several factors such as heat-exchange processes between skin, inner tissues, and vasculature as well as on metabolic activity and sympathetic and parasympathetic activity. As a result, its distribution may provide evidence of the centralization's progress due to peripheral hypoperfusion (restriction of blood flow to vital organs at the expense of peripheral organs) [15].

In 2014, Pereira et al. analyzed the capability of IRT (a) to detect acute impairments of body circulation and perfusion as well as (b) to monitor the progress of temperature centralization in a porcine animal model of acute lung injury (ALI) [15]. For that, two new indices (standard deviation and $\Delta T/\Delta x$) were developed. They aimed to quantify peripheral temperature gradients and, thus, peripheral perfusion [15].

In this study, ALI, one of the major causes leading to SIRS and sepsis, was experimentally induced in six female piglets. To evaluate the progress of skin temperature distribution, 15 measurements were performed with a long wave infrared camera at different points of time (approximately at two-hourly intervals). The thermograms were acquired with a VARIOCAM® hr head (InfraTec GmbH, Dresden, Germany), which presented a thermal sensitivity of 0.03 °C at 30 °C and a spatial resolution of 384 × 288 pixels [15].

As referred previously, two indices were proposed, standard deviation (SD) and $\Delta T/\Delta x$. The former corresponds to the standard deviation of the skin temperature distribution. The latter can be considered as a measure of the spatial temperature profile, i.e., it describes the change in temperature ΔT with the distance Δx between the body center (hottest point next to the coolish sternal region) and the most peripheral point visible in the thermogram (animal's paw). To evaluate the capability of IRT to detect acute impairments of body circulation and to monitor the progress of temperature centralization, both SD and $\Delta T/\Delta x$ were compared with clinical parameters such as shock index (SI),[7] mean arterial pressure (MAP), PaO_2 (partial pressure of oxygen), and Carrico index,[8] which are markers of circulatory impairments and oxygenation [15].

The results demonstrated that at the baseline measurement the body temperature of the piglets was uniformly distributed. However, with the progress of the disease's severity, the temperature gradient between center and periphery increased (temperature centralization) as a result of peripheral hypoperfusion. Figure 1.6 displays the development of the skin temperature distribution. Figure 1.6a and c represents the thermograms at two different time measurements, baseline and ALI 25 (last measurement). They show an increase of temperature profile due to hypoperfusion. Figure 1.6b, d shows the corresponding histograms. In general, differences of shape of the probability distributions between baseline and ALI were observed. At the baseline, the histograms presented a higher negative asymmetry and a higher kurtosis distribution, characterized by a sharper and longer peak. The latter means that the distribution is more clustered around the mean, which results in relatively smaller SDs, i.e., a more homogeneously distributed body temperature (Fig. 1.6a, b). During ALI the histograms presented smaller negative asymmetries and lower

---

[7] SI, a marker of shock, is the ratio of HR to systolic blood pressure. It is a effective marker for the initial assessment of sepsis.

[8] Carrico index, also denominated PaO_2/F_iO_2, is the ratio of arterial oxygen concentration to the fraction of inspired oxygen. In critical care medicine, this parameter describes the severity of pulmonary dysfunction.

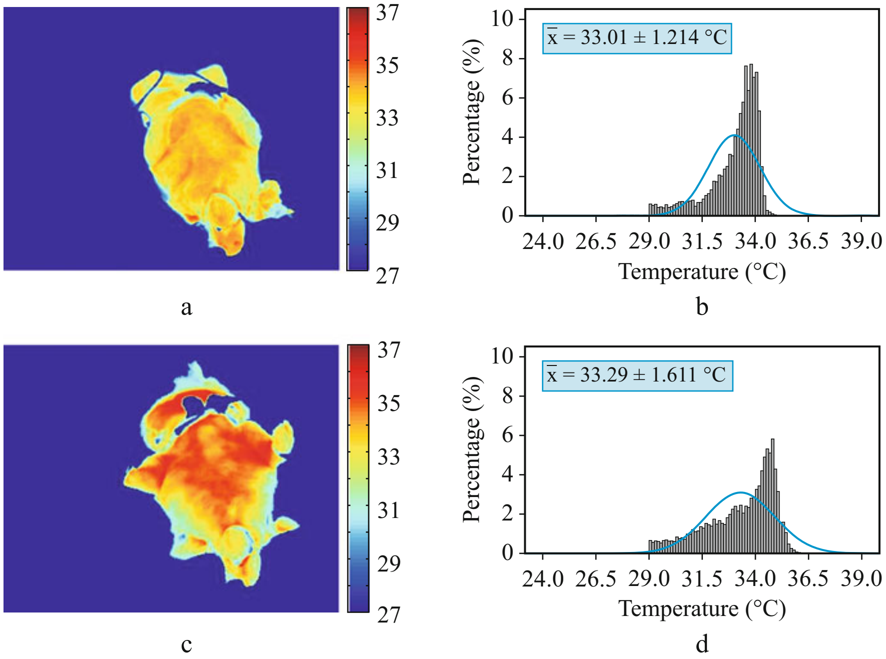

Fig. 1.6 Original thermograms at two different points of time: (**a**) Baseline and (**c**) ALI 25 (last measurement). Histograms representing the relative skin temperature distribution of the ROI (head, superior limbs and trunk) at these two time points: (**b**) Baseline and (**d**) ALI 25 (last measurement)

kurtosis distributions. A lower peak in the histogram denotes, on the contrary, that the distribution is less clustered around the mean. This can be translated into higher standard deviations and, consecutively, a heterogeneously distributed body temperature (temperature centralization) [15].

In addition, possible correlations between the two new indices and both SI and MAP were analyzed, as denoted in Table 1.4. Note that they are markers of circulatory impairments. The Pearson product-moment correlation evidenced a strong correlation between SD and SI as well as between $\Delta T/\Delta x$ and SI. Moreover, the same method demonstrated a strong negative correlation between both parameters, SD and MAP, and $\Delta T/\Delta x$ and MAP. The authors observed that the progress of the disease severity is accompanied by an increase in SD, $\Delta T/\Delta x$, and SI and a decrease in MAP. Commonly, sepsis and shock include hypotension and are characterized by an impaired blood flow to peripheral body tissues (hypoperfusion), which leads to temperature centralization (increased $\Delta T/\Delta x$ and SD). The Pearson product-moment correlation pointed out a moderate negative correlation between SD, $\Delta T/\Delta x$, SI and both PaO_2 and PF as well. Hypoperfusion is frequently accompanied by tissue hypoxia as there is an inability to meet the oxygen demands of the tissues [15].

Table 1.4 Pearson product-moment correlation between SD, $\Delta T/\Delta x$, SI and SI, MAP, PaO_2 and Carrico index [15]

		Standard deviation	$\Delta T/\Delta x$	SI
SI	Pearson correlation	$0.593^{a,b}$	$0.561^{a,b}$	–
	p-Value	<0.0005	<0.0005	–
MAP	Pearson correlation	$-0.587^{a,b}$	$-0.534^{a,b}$	$-0.519^{a,b}$
	p-Value	<0.0005	<0.0005	<0.0005
PaO_2	Pearson correlation	$-0.344^{a,c}$	$-0.334^{a,c}$	$-0.326^{a,c}$
	p-Value	0.004	0.005	0.007
PF ratio	Pearson correlation	$-0.315^{a,c}$	$-0.319^{a,c}$	$-0.326^{a,c}$
	p-Value	0.009	0.008	0.007

[a] Correlation is significant at the 0.01 level (two-tailed)

[b] Strong correlation $[0.40 < |r| < 0.70]$—according to Weinberg et al. [83]

[c] Moderate correlation $[0.30 < |r| < 0.39]$—according to Weinberg et al. [83]

In sum, the study demonstrated the ability of thermal imaging to monitor circulation and perfusion in a porcine animal model. The two new indices were capable of quantifying the course and severity of the disease.

1.4 Recent Advances in 3D Infrared Thermography

Infrared thermography is a powerful tool to gather information about temperature distribution on the surface of objects. A major disadvantage of thermographic cameras is that 3D bodies are represented by 2D images, which leads to the loss and distortion of information [84]. Especially for medical applications it can be very useful to visualize 3D representations of the temperature distribution of an object. This enables a more intuitive and precise analysis of the thermography data for the physician. Furthermore, the fusion of different image modalities becomes possible, for example, the fusion of thermal information with those of 3D models created by MRI scans [84, 85].

In order to create a 3D representation of the temperature distribution of a body surface, it is necessary to create a multitude of different 2D images that then are combined to obtain information about the depth of an object. A possible apparatus to create more than one image are stereo cameras. These consist of two cameras that create images of the same object from two different vantage points (like human binocular vision). Based on the relative positions of the object on these two different images, it is then possible to extract 3D information about the object, for example, the depth of a wound bed. Thermographic stereo cameras have been introduced in studies for breast cancer detection [86] and diabetic foot disease [87]. These devices generate information about the depth of surface structures, nevertheless it is not possible to produce a whole 3D surface model. A more sophisticated approach poses the recording of images from different angles. A major advantage of this technique is that regular infrared cameras can be used by taking images from the same object from different locations. For example, it is possible to generate a temperature map of the human head by taking four pictures with the same camera (one frontal image, one image of the left side, one image of the back, one image of the right side). These four 2D projections then have to be combined with an existing 3D model from another imaging modality. This could be a 3D scanning system that generates spatial models as well as the 3D models that are obtained by MRI or CT scans. The infrared images then are registered onto the 3D model. This registration process includes multiple image processing calculations that will not be discussed here. The resulting model then carries the combined 3D information of both imaging modalities [88].

MRI or CT scans are used to create 3D models of a variety of body parts like the brain, bone structures, or the heart in everyday clinical practice. These models contain anatomical information for medical diagnostics, for example, information about the integrity of bones and vessel walls as well as the location and size of tumors. Infrared images on the other hand are used to provide physiological information and therefore complement the anatomical information of MRI and CT scans. Possible medical applications lie in sports medicine as well as in tumor diagnostics as well as in breast cancer diagnostics, where a 3D model of the breast can be very useful to precisely detect regions of possible tumor development. The regions of inflammation detected by IRT can be mapped on the 3D model of a fracture and increased hemodynamics could provide crucial information about the development of a tumor that has been scanned with MRI.

1.5 Summary

The use and the fields of applications of thermal imaging have been growing throughout the last decades. Consecutive innovations in the production of infrared detectors made IRT an accurate and sensitive technology. The spatial resolution allied to the high sensitivity of infrared cameras contributed to their increasing use in medicine. Studies indicate the potential of thermal imaging in the diagnosis of breast cancer, rheumatic disease, chronic wounds, among others. In addition, IRT has demonstrated its potential as a monitoring technique (HR, RR, and perfusion), not only because of its sensitivity but also because is a passive and non-invasive method, which does not need a light source. In the last years, some advances in 3D thermal imaging were patent. Three-dimensional representations enable a more intuitive and precise visualization of body temperature distribution. In addition, more information can be achieved by combining 3D thermal imaging with other 3D models, for instance, from CT or MRI.

References

1. R. Berz et al., *Thermografie Kolloquium 2007* (2007)
2. B.B. Lahiri, S. Bagavathiappan, T. Jayakumar, J. Philip, Infrared Phys. Technol. **55**(4), 221 (2012)
3. E. Ring, K. Ammer, Physiol. Meas. **33**(3), R33 (2012)
4. C. Hildebrandt, C. Raschner, K. Ammer, Sensors (Basel) **10**(5), 4700 (2010)
5. M. Planck, *The Theory of Heat Radiation* (P. Blakiston's Son & Co., Philadelphia, 1914)
6. M. Planck, Ann. Phys. **4**, 553 (1901)
7. B.F. Jones, IEEE Trans. Med. Imaging **17**(6), 1019 (1998)
8. J. Steketee, Phys. Med. Biol. **18**(5), 686 (1973)
9. J.J. van Netten, J.G. van Baal, C. Liu, F. van der Heijden, S.A. Bus, J. Diabetes Sci. Technol. **7**(5), 1122 (2013)
10. S. Bagavathiappan, B.B. Lahiri, T. Saravanan, J. Philip, T. Jayakumar, Infrared Phys. Technol. **60**, 35 (2013)
11. B.F. Jones, P. Plassmann, IEEE Eng. Med. Biol. Mag. **21**(6), 41 (2002)
12. R. Resmini, A. Conci, L.F. da Silva, G.O. Sequeiros, F. Araújo, C. de Araújo, A.d.S. Araújo, R. Rodríguez-Ramos, F. Lebon, in *Application of Infrared to Biomedical Sciences*, 1st edn., ed. by E.Y. Ng, M. Etehadtavakol (Springer, Berlin, 2017)
13. Y. Chen, B. Kateb, *Neurophotonics and Brain Mapping* (CRC Press, Boca Raton, 2017)
14. F.S. Nahm, Korean J. Pain **26**(3), 219 (2013)
15. C.B. Pereira, M. Czaplik, N. Blanik, R. Rossaint, V. Blazek, S. Leonhardt, Biomed. Opt. Express **5**(4), 1075 (2014)
16. C. Hildebrandt, K. Zeilberger, E.F.J. Ring, C. Raschner, The application of medical infrared thermography in sports medicine, in *An International Perspective on Topics in Sports Medicine and Sports Injury (InTech, 2012)*
17. M. Kontos, R. Wilson, I. Fentiman, Clin. Radiol. **66**(6), 536 (2011)
18. V. Umadevi, S.V. Raghavan, S. Jaipurkar, Indian J. Med. Res. **134**(5), 725 (2011)
19. S.P. Niehof, F.J. Huygen, R.W. van der Weerd, M. Westra, F.J. Zijlstra, Biomed. Eng. Online **5**, 30 (2006)
20. A. Gardiner, R. Florin, C. Haber, in *Proceedings of Light-Activated Tissue Regeneration and Therapy Conference*, vol. 12, ed. by R. Waynant, D. Tata. Lecture Notes in Electrical Engineering (Springer, Boston, 2008), pp. 283–292
21. C.W. Cho, F.S. Nahm, E. Choi, P.B. Lee, I.K. Jang, C.J. Lee, Y.C. Kim, S.C. Lee, Medicine (Baltimore) **95**(52), e5548 (2016). https://doi.org/10.1097/MD.0000000000005548
22. M. Bharara, J.E. Cobb, D.J. Claremont, Int. J. Low. Extrem. Wounds **5**(4), 250 (2006)
23. J.H. Tan, E.Y.K. Ng, U. Rajendra Acharya, C. Chee, Infrared Phys. Technol. **53**(2), 120 (2010)
24. S. Matteoli, E. Favuzza, L. Mazzantini, P. Aragona, S. Cappelli, A. Corvi, R. Mencucci, Physiol. Meas. **38**(8), 1503 (2017). https://doi.org/10.1088/1361-6579/aa78bd
25. N. Zaproudina, Z. Ming, O.O.P. Hänninen, J. Manip. Physiol. Ther. **29**(3), 219 (2006)
26. E.F. Ring, P.A. Dieppe, P.A. Bacon, Br. J. Clin. Pract. **35**(7–8), 263 (1981)
27. G. Varjú, C.F. Pieper, J.B. Renner, V.B. Kraus, Rheumatology (Oxford) **43**(7), 915 (2004)
28. A.E. Denoble, N. Hall, C.F. Pieper, V.B. Kraus, Clin. Med. Insights Arthritis Musculoskelet. Disord. **3**, 69 (2010)
29. S. Bagavathiappan, T. Saravanan, J. Philip, T. Jayakumar, B. Raj, R. Karunanithi, T.M.R. Panicker, M.P. Korath, K. Jagadeesan, J. Med. Phys. **34**(1), 43 (2009). https://doi.org/10.4103/0971-6203.48720
30. C.L. Huang, Y.W. Wu, C.L. Hwang, Y.S. Jong, C.L. Chao, W.J. Chen, Y.T. Wu, W.S. Yang, J. Vasc. Surg. **54**(4), 1074 (2011). https://doi.org/10.1016/j.jvs.2011.03.287

31. E. Staffa, V. Bernard, L. Kubicek, R. Vlachovsky, D. Vlk, V. Mornstein, A. Bourek, R. Staffa, Vascular **25**(1), 42 (2017). https://doi.org/10.1177/1708538116640444
32. M.J. Lim, S.R. Kwon, K.H. Jung, K. Joo, S.G. Park, W. Park, J. Korean Med. Sci. **29**(4), 502 (2014). https://doi.org/10.3346/jkms.2014.29.4.502
33. R. Lasanen, E. Piippo-Savolainen, T. Remes-Pakarinen, L. Kröger, A. Heikkilä, P. Julkunen, J. Karhu, J. Töyräs, Physiol. Meas. **36**(2), 273 (2015). https://doi.org/10.1088/0967-3334/36/2/273
34. B. Lerkvaleekul, S. Jaovisidha, W. Sungkarat, N. Chitrapazt, P. Fuangfa, T. Ruangchaijatuporn, S. Vilaiyuk, Physiol. Meas. **38**(5), 691 (2017). https://doi.org/10.1088/1361-6579/aa63d8
35. J.Y. Park, J.K. Hyun, J.B. Seo, J. Shoulder Elbow Surg. **16**(5), 548 (2007)
36. V. Dini, P. Salvo, A. Janowska, F. Di Francesco, A. Barbini, M. Romanelli, Wounds **27**(10), 274 (2015)
37. E. Keenan, G. Gethin, L. Flynn, D. Watterson, G.M. O'Connor, Physiol. Meas. **38**(6), 1104 (2017)
38. A.A. Wahab, M.I.M. Salim, M.N.C. Aziz, in *Application of Infrared to Biomedical Sciences*, ed. by E.Y. Ng, M. Etehadtavakol. Series in BioEngineering (Springer, Singapore, 2017), pp. 109–131
39. R. Lawson, Can. Med. Assoc. J. **75**(4), 309 (1956)
40. R. Amalric, D. Giraud, C. Altschuler, F. Amalric, J.M. Spitalier, H. Brandone, Y. Ayme, A.A. Gardiol, Prog. Clin. Biol. Res. **107**, 269 (1982)
41. Z.S. Deng, J. Liu, *2005 IEEE Engineering in Medicine and Biology 27th Annual Conference* (2005), pp. 7525–7528
42. L. Boquete, S. Ortega, J.M. Miguel-Jiménez, J.M. Rodríguez-Ascariz, R. Blanco, J. Med. Syst. **36**(1), 103 (2012)
43. E.F. Ring, Bibl. Radiol. **1**(6), 97 (1975)
44. A.J. Collins, E.F. Ring, J.A. Cosh, P.A. Bacon, Ann. Rheum. Dis. **33**(2), 113 (1974)
45. E.F. Ring, A.J. Collins, P.A. Bacon, J.A. Cosh, Ann. Rheum. Dis. **33**(4), 353 (1974)
46. M. Frize, C. Adéa, P. Payeur, G. Di Primio, J. Karsh, A. Ogungbemile, *Proceedings of SPIE*, vol. 7962 (2011), pp. 79620M–79620M-11
47. C.L. Wu, K.L. Yu, H.Y. Chuang, M.H. Huang, T.W. Chen, C.H. Chen, J. Manip. Physiol. Ther. **32**(4), 287 (2009)
48. P.C. Vecchio, A.O. Adebajo, M.D. Chard, P.P. Thomas, B.L. Hazleman, Clin. Rheumatol. **11**(3), 382 (1992)
49. P.B. Morgan, A.B. Tullo, N. Efron, Eye (London) **9**(Pt 5), 615 (1995)
50. T.C. Chang, Y.L. Hsiao, S.L. Liao, Graefes Arch. Clin. Exp. Ophthalmol. **246**(1), 45 (2008)
51. C.K. Sen, G.M. Gordillo, S. Roy, R. Kirsner, L. Lambert, T.K. Hunt, F. Gottrup, G.C. Gurtner, M.T. Longaker, Wound Repair Regen. **17**(6), 763 (2009). https://doi.org/10.1111/j.1524-475X.2009.00543.x
52. R.N. Lawson, J.P. Gaston, Ann. N. Y. Acad. Sci. **121**(1), 90 (1964)
53. G.L. Hansen, E.M. Sparrow, N. Kommamuri, P.A. Iaizzo, Wound Repair Regen. **4**(3), 386 (1996)
54. V. Falanga, L.J. Saap, A. Ozonoff, Dermatol. Ther. **19**(6), 383 (2006)
55. M. Fierheller, R.G. Sibbald, Adv. Skin Wound Care **23**(8), 369 (2010)
56. M.A. Cretikos, R. Bellomo, K. Hillman, J. Chen, S. Finfer, A. Flabouris, Med. J. Aust. **188**(11), 657 (2008)
57. K.E. Philip, E. Pack, V. Cambiano, H. Rollmann, S. Weil, J. O'Beirne, J. Clin. Monit. Comput. **29**(4), 455 (2015)
58. R. Murthy, I. Pavlidis, P. Tsiamyrtzis, *Engineering in Medicine and Biology Society, 2004. IEMBS'04. 26th Annual International Conference of the IEEE*, vol. 1 (IEEE, Piscataway, 2004), pp. 1196–1199

59. J. Fei, I. Pavlidis, *Engineering in Medicine and Biology Society, 2007. EMBS 2007. 29th Annual International Conference of the IEEE* (IEEE, Piscataway, 2007), pp. 250–253
60. J. Fei, I. Pavlidis, IEEE Trans. Biomed. Eng. **57**(4), 988 (2010)
61. S.Y. Chekmenev, H. Rara, A.A. Farag, *The First International Conference on Graphics, Vision, and Image Processing (GVIP)*, Cairo (2005), pp. 107–112
62. M. Yang, Q. Liu, T. Turner, Y. Wu, *IEEE Conference on Computer Vision and Pattern Recognition, 2008. CVPR 2008* (IEEE, Piscataway, 2008), pp. 1–8
63. J.N. Murthy, J. van Jaarsveld, J. Fei, I. Pavlidis, R.I. Harrykissoon, J.F. Lucke, S. Faiz, R.J. Castriotta, Sleep **32**(11), 1521 (2009)
64. A.K. Abbas, K. Heimann, K. Jergus, T. Orlikowsky, S. Leonhardt, Biomed. Eng. Online **10**(1), 93 (2011)
65. F. Al-Khalidi, R. Saatchi, H. Elphick, D. Burke, Am. J. Eng. Appl. Sci. **4**(4), 586 (2011)
66. G.F. Lewis, R.G. Gatto, S.W. Porges, Psychophysiology **48**(7), 877 (2011)
67. C.B. Pereira, X. Yu, M. Czaplik, R. Rossaint, V. Blazek, S. Leonhardt, Biomed. Opt. Express **6**(11), 4378 (2015)
68. C.B. Pereira, X. Yu, M. Czaplik, V. Blazek, B. Venema, S. Leonhardt, J. Clin. Monit. Comput. **31**(6), 1241–1254 (2017)
69. S.Y. Chekmenev, A.A. Farag, E.A. Essock, *2007 IEEE Conference on Computer Vision and Pattern Recognition* (2007), pp. 1–6
70. M. Garbey, N. Sun, A. Merla, I. Pavlidis, IEEE Trans. Biomed. Eng. **54**(8), 1418 (2007)
71. F.N.v.d. Vosse, N. Stergiopulos, Annu. Rev. Fluid Mech. **43**(1), 467 (2011)
72. T.R. Gault, A.A. Farag, *2013 IEEE Conference on Computer Vision and Pattern Recognition Workshops (CVPRW)* (2013), pp. 336–341
73. R.P. Dellinger, M.M. Levy, J.M. Carlet, J. Bion, M.M. Parker, R. Jaeschke, K. Reinhart, D.C. Angus, C. Brun-Buisson, R. Beale, T. Calandra, J.F. Dhainaut, H. Gerlach, M. Harvey, J.J. Marini, J. Marshall, M. Ranieri, G. Ramsay, J. Sevransky, B.T. Thompson, S. Townsend, J.S. Vender, J.L. Zimmerman, J.L. Vincent, International Surviving Sepsis Campaign Guidelines Committee, American Association of Critical-Care Nurses, American College of Chest Physicians, American College of Emergency Physicians, Canadian Critical Care Society, European Society of Clinical Microbiology and Infectious Diseases, European Society of Intensive Care Medicine, European Respiratory Society, International Sepsis Forum, Japanese Association for Acute Medicine, Japanese Society of Intensive Care Medicine, Society of Critical Care Medicine, Society of Hospital Medicine, Surgical Infection Society, World Federation of Societies of Intensive and Critical Care Medicine, Crit. Care Med. **36**(1), 296 (2008)
74. M. Odeh, Postgrad. Med. J. **72**(844), 66 (1996)
75. S.C.P.L. Shiramizo, A.R. Marra, M.S. Durão, Â.T. Paes, M.B. Edmond, O.F. Pavão dos Santos, PLoS ONE **6**(11), e26790 (2011)
76. J.H. Wu, C.Y. Chen, P.N. Tsao, W.S. Hsieh, H.C. Chou, Pediatr. Neonatol. **50**(3), 88 (2009)
77. D.C. Angus, W.T. Linde-Zwirble, J. Lidicker, G. Clermont, J. Carcillo, M.R. Pinsky, Crit. Care Med. **29**(7), 1303 (2001)
78. G.S. Martin, D.M. Mannino, S. Eaton, M. Moss, N. Engl. J. Med. **348**(16), 1546 (2003)
79. F.B. Mayr, S. Yende, D.C. Angus, Virulence **5**(1), 4 (2014)
80. J.E. Lawn, S. Cousens, J. Zupan, Lancet Neonatal Survival Steering Team, Lancet **365**(9462), 891 (2005)
81. T. Koch, S. Geiger, M.J. Ragaller, J. Am. Soc. Nephrol. **12**(Suppl. 17), S53 (2001)
82. A. Kumar, D. Roberts, K.E. Wood, B. Light, J.E. Parrillo, S. Sharma, R. Suppes, D. Feinstein, S. Zanotti, L. Taiberg, D. Gurka, A. Kumar, M. Cheang, Crit. Care Med. **34**(6), 1589 (2006)
83. S.L. Weinberg, S.K. Abramowitz, *Statistics Using SPSS: An Integrative Approach* (Cambridge University Press, Cambridge, 2008)

84. M. Unger, A. Franke, C. Chalopin, Curr. Dir. Biomed. Eng. **2**(1), 369 (2016)
85. M.A. de Souza, I.J. Sanches, H.R. Gamba, P. Nohama, Conf. Proc. IEEE Eng. Med. Biol. Soc. **2013**, 3371 (2013)
86. I. Grubisic, L. Gjenero, T. Lipic, I. Sovic, T. Skala, *Proceedings of the 34th International Convention MIPRO* (2011), pp. 269–273
87. S. Barone, A. Paoli, A.V. Razionale, *XVIII Congreso Internactional de Ingenieria Grafica*, Sitges (2006)
88. M.A. de Souza, A.G. Krefer, G.B. Borba, T.M. Centeno, H.R. Gamba, Conf. Proc. IEEE Eng. Med. Biol. Soc. **2015**, 2395 (2015)